Available online at www.sciencedirect.com
SCIENCE DIRECT®
Physics Letters A 344 (2005) 432–440
PHYSICS LETTERS A
www.elsevier.com/locate/pla

Domain walls and textured vortices in a two-component Ginzburg–Landau model

S. Madsen [a,*], Yu.B. Gaididei [b], P.L. Christiansen [c], N.F. Pedersen [a]

[a] *Ørsted•DTU, Electric Power Engineering, The Technical University of Denmark, DK-2800 Kgs. Lyngby, Denmark*
[b] *Bogolyubov Institute for Theoretical Physics, 252143 Kiev, Ukraine*
[c] *Informatics and Mathematical Modelling and Department of Physics, The Technical University of Denmark, DK-2800 Kgs. Lyngby, Denmark*

Received 21 April 2005; accepted 27 June 2005

Available online 5 July 2005

Communicated by A.R. Bishop

Abstract

We look for domain wall and textured vortex solutions in a two-component Ginzburg–Landau model inspired by two-band superconductivity. The two-dimensional two-component model, with equal coherence lengths and no magnetic field, shows some interesting properties. In the absence of a Josephson type coupling between the two order parameters a "textured vortex" is found by analytical and numerical solution of the Ginzburg–Landau equations. With a Josephson type coupling between the two order parameters we find the system to split up in two domains separated by a domain wall, where the order parameter is depressed to zero.

1. Introduction

The long list of physical systems where topological defects plays an important role includes such seemingly different fields as superconductivity [1], cosmology [2], and singular optics [3], to name a few. In cosmology, e.g., topological defects in the form of vortices have been considered as the seed of galaxy formation by their gravitational field in various different gravitational theories [4]. In singular optics, e.g., optical vortices [5] has been considered in connection with pattern formation in lasers [6]. The study of topological defects in field theoretic models are thus of broad physical interest, though we are here inspired by two-gap superconductivity.

The most famous topological defect in superconductivity is without doubt the Abrikosov vortex, but different types may also be considered. We shall here use a simplified version of the two-component Ginzburg–Landau theory to consider domain walls

* Corresponding author.
E-mail address: soeren@madsen2themax.dk (S. Madsen).

0375-9601/$ – see front matter
doi:10.1016/j.physleta.2005.06.095

and non-Abrikosov types of vortices. The model is inspired by the discovery of superconductivity in MgB_2 a few years ago [7]. Of particular, interest is the presence of two energy gaps [8] leading to two order parameters in a Ginzburg–Landau type of theory [9]. This kind of multi-component Ginzburg–Landau theory has previously been discussed by several authors [10]. In the present work we consider a simplified version of the two-component Ginzburg–Landau theory, in which magnetic effects are neglected, order parameters are assumed to have equal coherence lengths, and the case of an isotropic superconductor is considered. Even in this simple model, interesting features in the form of topological defects are found.

The Letter is organized in the following way: in Section 2, starting from the free energy functional for the two-component Ginzburg–Landau model we derive analytical solutions corresponding to domain walls and textured vortices. In Section 3 we solve the coupled partial differential equations numerically and discuss the relationship to the analytical results obtained in Section 2. Section 4 contains our conclusion.

2. Theory

We consider the two-dimensional static case described by the free energy functional

$$F = \int d^2x \bigg(\frac{1}{2}(\nabla\psi_1)(\nabla\psi_1)^* + \frac{1}{2}(\nabla\psi_2)(\nabla\psi_2)^* + V\big(|\psi_1|, |\psi_2|\big) - \eta\big(\psi_1^*\psi_2 + \psi_1\psi_2^*\big)\bigg), \tag{1}$$

where ψ_1 and ψ_2 are the two normalized order parameters, η is the strength of the Josephson type coupling between the order parameters, and V is the standard 4th order Ginzburg–Landau potential in each of the order parameters

$$V\big(|\psi_1|, |\psi_2|\big) = -\frac{1}{2}\big(|\psi_1|^2 + |\psi_2|^2\big) + \frac{1}{4}\big(|\psi_1|^4 + |\psi_2|^4\big), \tag{2}$$

where we have assumed equal coherence lengths for the two order parameters.

2.1. Domain walls

We first consider a domain wall linking two phases. Assuming real order parameters and $\psi_1 = \pm\psi_2$, the equations

$$\nabla^2\psi_1 + (1 \pm 2\eta)\psi_1 - \psi_1^3 = 0 \tag{3}$$

is obtained from the Euler–Lagrange equations. Considering the case where ψ_1 is independent of the y-coordinate, a solution to the above equation becomes

$$\psi_1 = \sqrt{1 \pm 2\eta}\tanh\bigg(\sqrt{\frac{(1 \pm 2\eta)}{2}}x\bigg), \tag{4}$$

describing a domain wall located along the y axis. Note, for $\eta > 0$ ($\eta < 0$) the solution with $\psi_1 = \psi_2$ ($\psi_1 = -\psi_2$) has a lower energy than the solution with $\psi_1 = -\psi_2$ ($\psi_1 = \psi_2$).

Note that the domain wall is similar to a SNS Josephson π-junction [13].

2.2. Textured vortices

We now consider textured vortex solutions. Assuming real order parameters, we may write

$$\psi_1 = F(x, y)\cos\phi(x, y), \qquad \psi_2 = F(x, y)\sin\phi(x, y), \tag{5}$$

where F and ϕ denote amplitude and phase, respectively. The field equations then become

$$\nabla\cdot\big(F^2\nabla\phi\big) + 2\eta F^2\cos 2\phi + \frac{F^4}{4}\sin 4\phi = 0 \tag{6}$$

and

$$\nabla^2 F - F(\nabla\phi)^2 = \frac{F^3}{4}(3 + \cos 4\phi) - F(1 + 2\eta\sin 2\phi). \tag{7}$$

An approximate analytical solution to Eqs. (6) and (7) in the far-field is obtained by assuming vanishing derivatives of F in Eq. (7), leading to $F = 0$ or

$$F^2 = \frac{4(1 + 2\eta\sin 2\phi - (\nabla\phi)^2)}{3 + \cos 4\phi}. \tag{8}$$

Inserting the latter expression into Eq. (6) and neglecting ∇F, we obtain the approximative equation

$$\nabla^2\phi + 4\eta\cos 2\phi + \frac{1}{2}\sin 4\phi = 0, \tag{9}$$

valid for $\phi \approx \pi/4 + n\pi/2$ with $n = 1, 2, \ldots$ (i.e., $\cos 4\phi \approx -1$).

Requiring two-fold symmetry we get the boundary conditions

$$\left|\psi_i(r,\chi)\right| = \left|\psi_i(r,\chi+n\pi)\right|, \quad i = 1,2, \tag{10}$$

where $n = 1, 2, \ldots$, thus

$$\phi(r,\chi) = \phi(r,\chi+n\pi) + n\pi, \tag{11}$$

where (r,χ) are polar coordinates in the (x,y) plane.

In Appendix A we show that an approximative solution to Eqs. (9) and (11) may be written as

$$\phi = \frac{\pi}{4} \pm \tan^{-1}\left(\beta\,\mathrm{sc}\left(\frac{2K(m)}{\pi}\chi \,\middle|\, m\right)\right), \tag{12}$$

where $\mathrm{sc}(s|m)$ is the Jacobi elliptic function $\mathrm{sc} = \mathrm{sn}/\mathrm{cn}$ with modulus m [14], which is determined by solving

$$\frac{2K(m)}{\pi} = r\sqrt{\frac{4c}{2-m}}, \tag{13}$$

$K(m)$ being the complete elliptic integral of the first kind [14]. β and c are given by

$$\beta = \sqrt{\frac{4c}{2c+4\eta-1}\frac{1-m}{2-m}} \tag{14}$$

and

$$c = \frac{2-m}{2m}\left(\frac{2-m}{m} + \sqrt{\left(\frac{2-m}{m}\right)^2 - 1 + 16\eta^2}\right). \tag{15}$$

Thus, m depends on r as well as η.

For $\eta = 0$, the two-fold symmetric boundary conditions, Eq. (10), become four-fold symmetric, Eqs. (10) and (11) hold when n is half-integer, and

$$\phi = \tan^{-1}\left(\frac{\sinh(y/\sqrt{2})}{\sinh(x/\sqrt{2})}\right), \tag{16}$$

becomes an *exact* solution to Eq. (9) [11].

Figs. 1 and 2 show the analytical solution F, given by Eq. (8), and the vector $(\cos\phi, \sin\phi)$, ϕ given by Eq. (12), for zero and non-zero value of the Josephson type coupling strength, η. Comparing Figs. 1 and 2, we clearly see that the presence of the Josephson coupling term breaks the 4-fold symmetry.

3. Numerical solutions

To obtain numerical solutions, the partial differential equations resulting from the free energy functional in Eq. (1) are discretized using 2nd order finite differences. A spatial separation of 0.125 is used for the spatial derivatives. A temporal damping term is added. The resulting "time-dependent" equations are then solved by an Euler method. This relaxation procedure is continued until the energy difference, ΔF, between two subsequent time-steps is less than 10^{-7}. Neumann boundary conditions, $\mathbf{n}\cdot\nabla\psi_i = 0$ where $\mathbf{n}$ is a normal to the boundary and $i = 1, 2$, were choosen in agreement with usual Ginzburg–Landau simulations for zero magnetic field [12]. We consider a square and a circular[1] geometry. For brevity anti-vortex solutions are not discussed.

We first consider the textured vortex solutions for $\eta = 0$, described by Eqs. (8) and (16). Using this analytical far-field solution as initial conditions for the Euler procedure, we obtain the plots in the left column of Figs. 3 and 4. Note, the initial conditions in the square geometry has been rotated to fit the symmetry of the geometry. The overall agreement between these plots and the plots in Fig. 1 is quite good, except near the origin where the numerical solution has $F = 0$ which is far from the assumptions made in the derivation of Eqs. (8), (12) and (16).

Now, the solutions for $\eta \neq 0$ are obtained as function of "time" using again the Euler procedure with the relaxed numerical solutions for $\eta = 0$, just obtained, as initial conditions. The result is shown in Figs. 3 and 4. The left column is the initial conditions, the middle column is the solution at a selected time, and the right column is the numerical solution after convergence of the Euler procedure. We see the four-fold symmetric solution for $\eta = 0$ develops towards a two-fold symmetric solution for $\eta \neq 0$. The presence of the η-term changes the energy densities of the four phases, such that two of them has lower energy density than the other two, leading to a motion of the domain walls to minimize the area of the high-energy domains. This development occurs faster in the circular case (Fig. 4 shows only two domains at $t = 70$) than in the square

[1] Within the resolution of the square discretization of the spatial coordinates.

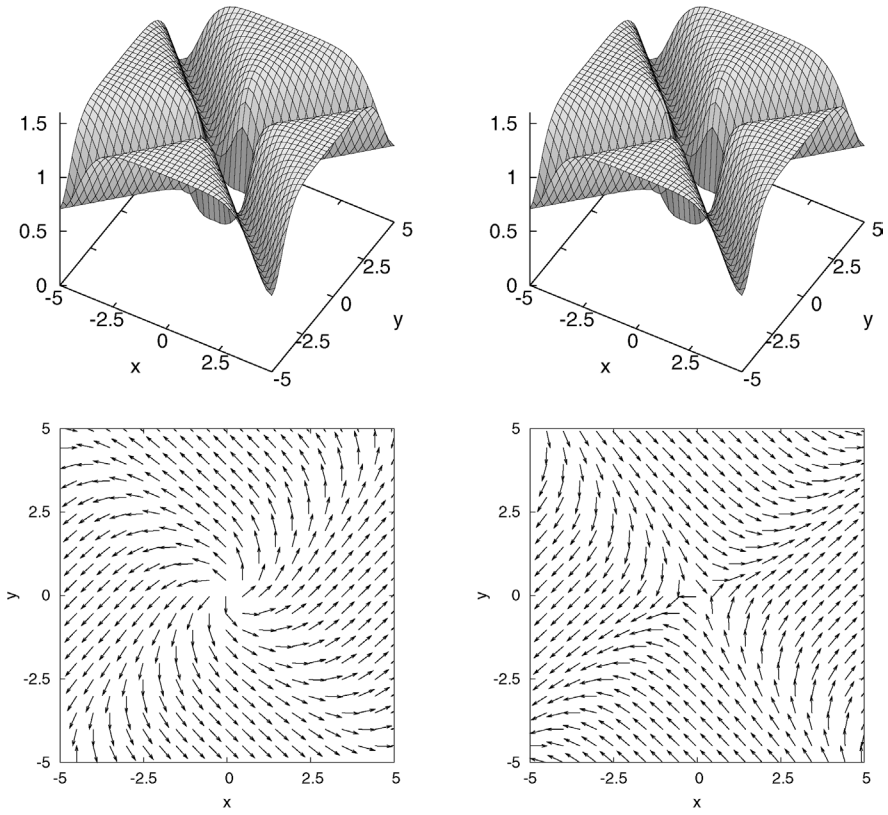

Fig. 1. Far-field solution. Top row: F given by Eq. (8). Bottom row: vector $(\cos\phi, \sin\phi)$ (not to scale). ϕ given by Eq. (12). $\eta = 0$. Left: vortex (+ in Eq. (12)). Right: anti-vortex (− in Eq. (12)). F^2 in Eq. (8) becomes negative near the origin, signaling the breakdown of the far-field assumption.

case (Fig. 3 still has all four domains at $t = 327$). The difference between the "dynamics" in the square and circular geometries is caused by the Neumann boundary conditions, which require that the domain walls are perpendicular to the boundary of the system. They counter-act the minimization of the high-energy domains in the square geometry. Thus, we see a complete elimination of the high energy domains for the circular case, while all four domains remain in the square case. From this it is evident that by changing η in the square geometry, the domain sizes may be changed.

To study the difference between the numerical solutions in Figs. 3 and 4, we calculate the winding number, n, given by [11]

$$2\pi n \equiv \oint_C \big(\partial_x \phi(x, y)\, dx + \partial_y \phi(x, y)\, dy\big), \tag{17}$$

where C is an arbitrary contour around the vortex and ϕ is defined in Eq. (5). For vortex and anti-vortex solutions n is an integer different from zero, n positive (negative) corresponds to a vortex (anti-vortex). In Fig. 5, we have plotted n as a function of "time" for the two cases corresponding to Figs. 3 and 4. As C we have choosen a circle, centered at the origin. Two different radii have been used in each case, $r = 7$ and $r = 11$. The figure shows, that in the square case the vortex remains (i.e., $n \approx 1$ as t increases) but for the circular case the vortex moves out of the system (i.e., $n \to 0$, after reaching a maximum value, as t increases). Note that n diverges from unity earlier for $r = 7$ than for $r = 11$ in agreement with the outwards vortex motion.

The Neumann boundary conditions used in the numerical simulations causes the difference between the dynamics of the square and circular geometries. For

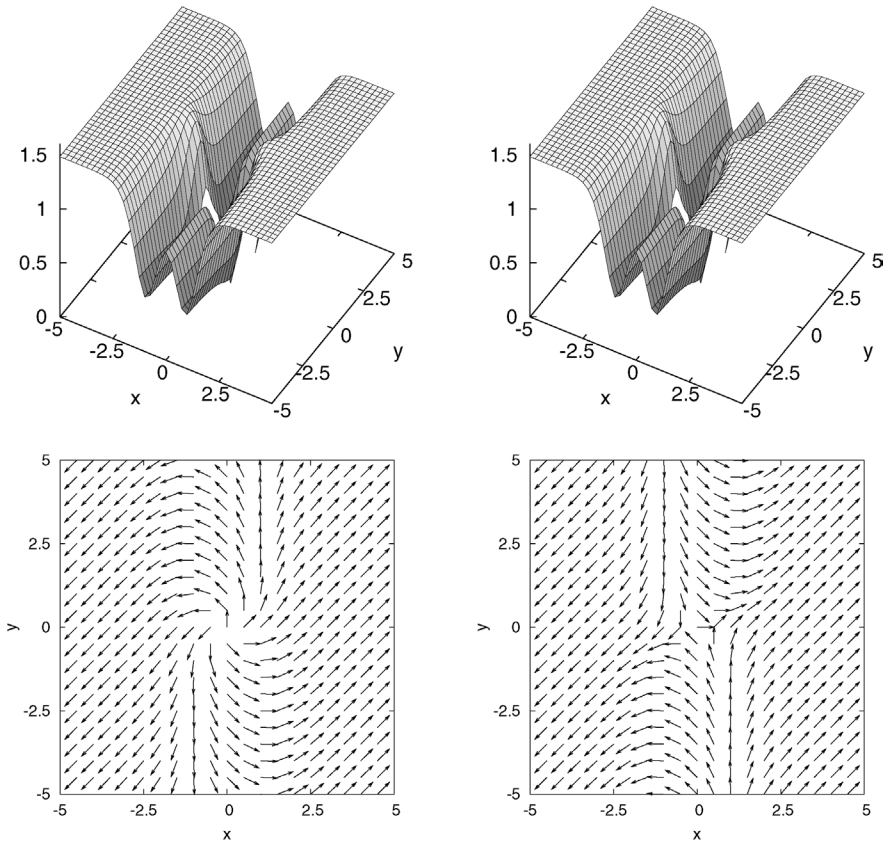

Fig. 2. Far-field solution. Top row: F given by Eq. (8). Bottom row: vector $(\cos\phi, \sin\phi)$ (not to scale). ϕ given by Eq. (12). $\eta = 0.05$. Left: vortex (+ in Eq. (12)). Right: anti-vortex (− in Eq. (12)). F^2 in Eq. (8) becomes negative near the origin, signaling the breakdown of the far-field assumption.

the circular system with a vortex at the exact center, the Neumann boundary conditions corresponds to an image anti-vortex located at infinity. When the vortex is not located exactly at the center, the image anti-vortex lies at a finite distance. The attraction between the vortex and the image anti-vortex results in a motion of the vortex along the domain wall. For the square case, the boundary conditions lead to multiple image anti-vortices located outside the system, thus creating a more stable state than in the circular geometry. Note, that for coarser discretization of the equations, we observe vortex motion also in the square system. Thus, the difference between the dynamics in the square and circular geometry is thus due to finite size effects which seem to play a major role.

For the circular geometry with $\eta = 0.05$ we get a system with only two phases linked by a domain wall. This is precisely the domain wall solution found in Eq. (4). To check this, we plot in Fig. 6 the expression given by Eq. (4) as well as $\psi_1(x, 0)$ from the data in the right column of Fig. 4. The agreement is seen to be excellent.

The solution for $\eta \neq 0$ plotted in Fig. 2 is not observed as a stationary state in our numerical simulations. However, the solution in the middle column of Figs. 3 and 4 and in the outer part of the 2nd and 4th quadrant of the square in the right column of Fig. 3 possess some resemblance to the analytical solution plotted in Fig. 2. The corresponding expression in Eq. (12) was derived for the static case near $F^2 = 2(1 \pm 2\eta)$. Thus, such a resemblance may not be expected to hold near the origin and along the domain wall (shown in Fig. 4) which separates the two low-energy phases, since F^2 is here very different from $2(1 \pm 2\eta)$.

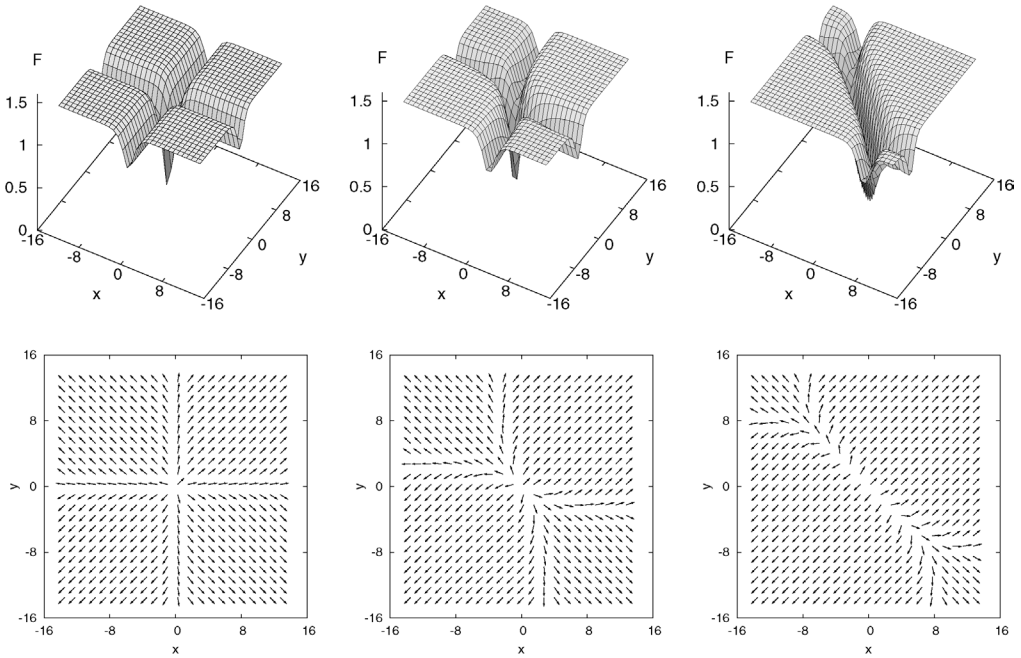

Fig. 3. Square geometry: "Time"-evolution of F (upper) and the vector $(\cos\phi, \sin\phi)$ (lower) for $\eta = 0.02$. Initial conditions: numerical solution for $\eta = 0$. Snapshots at: $t = 0$ (left, initial conditions), $t = 35$ (middle), and $t = 327$ (right, final stage).

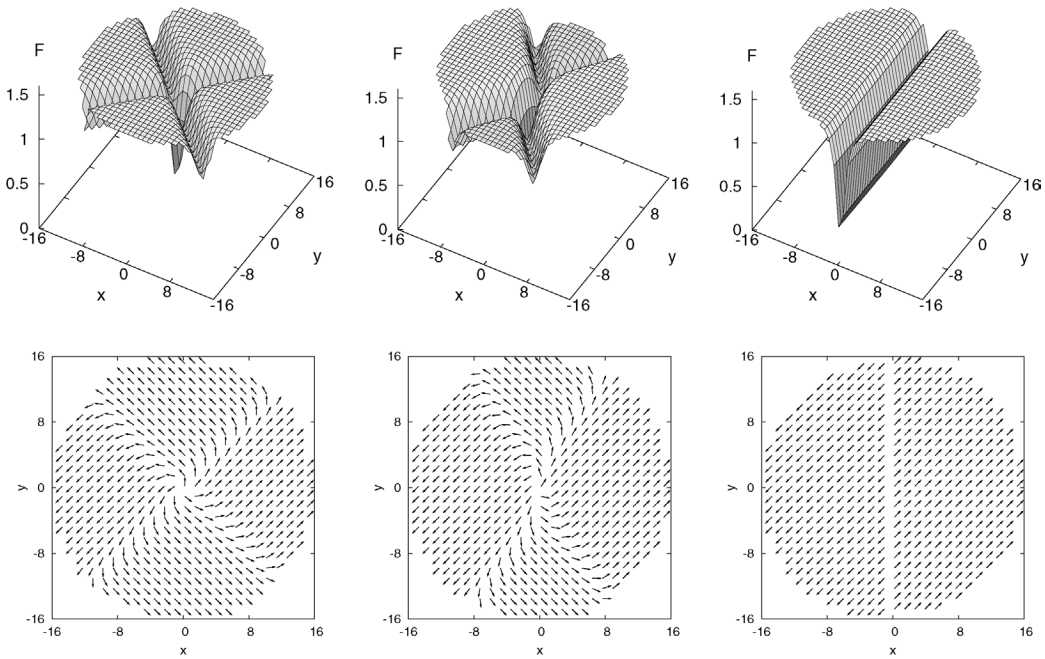

Fig. 4. Circular geometry: "Time"-evolution of F (upper) and the vector $(\cos\phi, \sin\phi)$ (lower) for $\eta = 0.05$. Initial conditions: numerical solution for $\eta = 0$. Snapshots at: $t = 0$ (left, initial conditions), $t = 14$ (middle), and $t = 70$ (right, final stage).

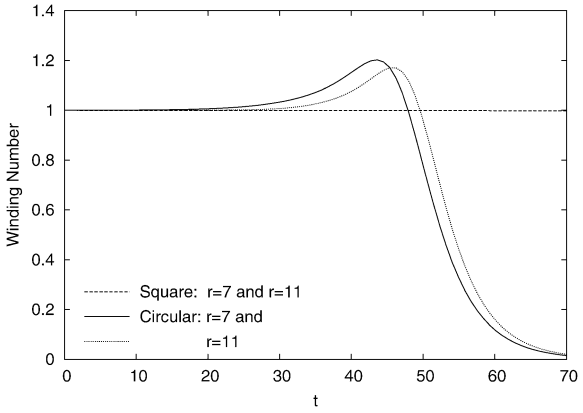

Fig. 5. Winding number, n, given by Eq. (17) for square (Fig. 3) and circular geometry (Fig. 4). In the square geometry, the vortex present at $t = 0$ remains in the system, i.e., $n \approx 1$ also for $t > 70$ (not shown). In the circular geometry the vortex disappears after approximately 70 time units.

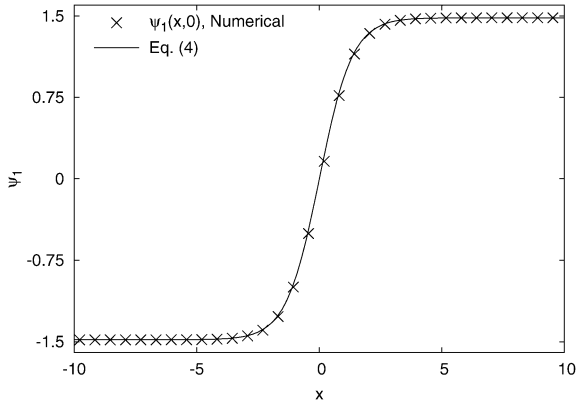

Fig. 6. $\psi_1(x, 0)$ from numerical solution in circular geometry (Fig. 4, $t = 70$, $\eta = 0.05$). The analytical domain wall solution in Eq. (4) fits the numerical data. Since $\eta > 0$, $\psi_1 = \psi_2$.

The average energy densities of the initial state (for $\eta = 0$) and final state (for $\eta \neq 0$) solutions considered in Figs. 3 and 4 are roughly 10%–20% higher than the energy density of the homogeneous state $\psi_1 = \pm\psi_2 = \sqrt{1 \pm 2\eta}$, thus the domain wall and textured vortex solutions are excited states.

4. Conclusion

Domain walls and textured vortices in a two-component Ginzburg–Landau model, inspired by two-gap superconductivity were investigated analytically and numerically. In particular, we study the effect of a Josephson type coupling term between the order parameters. Without Josephson coupling we find a "textured vortex" solution and for non-zero Josephson coupling this "textured vortex" develops into a domain wall. As a consequence the vortex is lost in the system. By changing the geometry of the system, we find that boundary effects may prevent escape of the vortex.

Acknowledgements

Support from the Danish STVF program "New superconductors: mechanisms, processes, and products" is acknowledged. S.M. would like to thank M. Milosevic and F.M. Peeters for hospitality and help with the numerics. Yu.B.G. acknowledges the hospitality of the DTU Physics Department as well as a Guest Professorship funded by Civilingeniør Frederik Christiansens Almennyttige Fond and MIDIT, SNF grant #21-02-0500.

Appendix A. Approximate solution of Eq. (9)

We consider

$$\nabla^2\phi + a\cos 2\phi + b\sin 4\phi = 0, \tag{A.1}$$

which for $a = 4\eta$ and $b = 1/2$ becomes Eq. (9). Following Ref. [11] we make the approximation $\nabla^2\phi \approx \phi''/r^2$ where primes denotes differentiation with respect to the angular coordinate, χ. Eq. (A.1) then reduces to

$$\frac{1}{r^2}\phi'' + a\cos 2\phi + b\sin 4\phi = 0, \tag{A.2}$$

which we shall solve subjected to the boundary conditions in Eq. (11). Introducing the auxiliary variable $\varphi \equiv \phi - \pi/4$ and integrating,

$$\frac{1}{2r^2}(\varphi')^2 + \frac{a}{2}\cos 2\varphi + \frac{b}{4}(\cos 4\varphi + 3) = c, \tag{A.3}$$

is obtained, where the integration constant is conveniently choosen as $c - 3b/4$. We limit ourselves to solutions where $c > a/2 + b > 0$, and introduce the auxiliary variable $t \equiv \tan\varphi$. Eq. (A.3) may now be re-

arranged as

$$\frac{dt}{\sqrt{(t^2+\alpha^2)(t^2+\beta^2)}} = \pm r\sqrt{2c+a-2b}\,d\chi, \quad \text{(A.4)}$$

which integrates into

$$\mathrm{F}\left(\tan^{-1}\tfrac{t}{\beta}|m\right) = \pm\alpha r\sqrt{2c+a-2b}(\chi-\chi_0), \quad \text{(A.5)}$$

where $\mathrm{F}(u|m)$ is the elliptic integral of the first kind with modulus m [14], given by $m=(\alpha^2-\beta^2)/\alpha^2$, χ_0 is an integration constant, and the roots of the 2nd degree polynomial in t^2

$$(c+a/2-b)t^4+2ct^2+c-a/2-b=0, \quad \text{(A.6)}$$

are denoted by $-\alpha^2$ and $-\beta^2$, respectively. They may be expressed as

$$\alpha = \sqrt{\frac{4c}{2c+a-2b}\frac{1}{2-m}} \quad \text{(A.7)}$$

and

$$\beta = \sqrt{\frac{4c}{2c+a-2b}\frac{1-m}{2-m}}. \quad \text{(A.8)}$$

Solving Eq. (A.5) for φ we get

$$\tan\varphi = \pm\beta\,\mathrm{sc}\left(\alpha r\sqrt{2c+a-2b}(\chi-\chi_0)|m\right). \quad \text{(A.9)}$$

Rewriting the boundary condition, Eq. (11), as $\tan\varphi(\chi+n\pi)=\tan\varphi(\chi)$ and using the periodicity of the Jacobi amplitude function [16], $\mathrm{am}(s+2nK(m)|m)=\mathrm{am}(s|m)+n\pi$, we get

$$\alpha r\sqrt{2c+a-2b} = \frac{2}{\pi}K(m). \quad \text{(A.10)}$$

From this equation, we may determine m, using

$$c = b\frac{2-m}{m}\left(\frac{2-m}{m} \pm \sqrt{\left(\frac{2-m}{m}\right)^2 - 1 + \frac{a^2}{4b^2}}\right), \quad \text{(A.11)}$$

which is obtained by insertion of Eqs. (A.7) and (A.8) into $m=(\alpha^2-\beta^2)/\alpha^2$.

In the limit $m\to 1$ Eqs. (A.7), (A.8) and (A.11) yield

$$\lim_{m\to1}\alpha = \frac{a+2b}{a}, \quad \text{(A.12)}$$

$$\lim_{m\to1}\beta = 0, \quad \text{(A.13)}$$

$$\lim_{m\to1} c = \begin{cases} a/2+b, \\ a/2+b/2. \end{cases} \quad \text{(A.14)}$$

Since $\lim_{m\to1}K(m)=\infty$, we get from Eq. (A.10) that $m\to1$ must correspond to $r\to\infty$. This tells us, that in order to satisfy $c>a/2+b$ for all r, $+$ sign in Eq. (A.11) must be choosen.

For $a=4\eta$, $b=1/2$ and $\chi_0=0$, Eqs. (A.9), (A.7), (A.8), (A.10), and (A.11) yield the solution given by Eqs. (12)–(15).

For $a=0$ and $b=1/2$ Eq. (A.1) reduces to

$$\nabla^2\phi + \frac{1}{2}\sin 4\phi = 0, \quad \text{(A.15)}$$

which has the solution [15]

$$\phi = \pm\frac{1}{2}\,\mathrm{am}\left(\frac{4K(m)}{\pi}\chi\,\middle|\,\mu\right), \quad \text{(A.16)}$$

where $\mathrm{am}(s|\mu)$ is the Jacobi elliptic amplitude function with modulus μ, where μ must be determined from[2]

$$\sqrt{\frac{2}{\mu}}r\pi = 4K(\mu). \quad \text{(A.17)}$$

The general solution in Eqs. (A.9), (A.7), (A.8), (A.10), and (A.11) reduces to Eqs. (A.16) and (A.17) when $\chi_0=-\pi/4$ and

$$m = \frac{4\sqrt{\mu}}{(1+\sqrt{\mu})^2}. \quad \text{(A.18)}$$

References

[1] A.A. Abrikosov, J. Exp. Theor. Phys. (USSR) 5 (1957) 1174.
[2] A. Vilenkin, E.P.S. Shellard, Cosmic Strings and Other Topological Defects, Cambridge Univ. Press, Cambridge, 1994.
[3] M.S. Soskin, M.V. Vasnetsov, Prog. Opt. 42 (2001) 219.
[4] See, e.g., Y. Verbin, S. Madsen, A.L. Larsen, M. Christensen, Phys. Rev. D 65 (2002) 063503;
Y. Verbin, S. Madsen, A.L. Larsen, Phys. Rev. D 67 (2003) 085019, and references therein.
[5] P. Coullet, L. Gil, F. Rocca, Opt. Commun. 73 (1989) 403.
[6] C.O. Weiss, M. Vaupel, K. Staliunas, G. Slekys, V.B. Taranenko, Appl. Phys. B (1999) 151.
[7] J. Nagamatsu, N. Nakagawa, T. Muranaka, Y. Zenitani, J. Akimitsu, Nature 410 (2001) 63.
[8] A. Brinkman, A.A. Golubov, H. Rogalla, O.V. Dolgov, J. Kortus, Y. Kong, O. Jepsen, O.K. Andersen, Phys. Rev. B 65 (2002) 180517.
[9] M.E. Zhitomirsky, V.H. Dao, Phys. Rev. B 69 (2004) 054508.

[2] Please note, in Ref. [15] there is a misprint in this expression.

[10] See, e.g., E. Babaev, Phys. Rev. Lett. 89 (2002) 067001;
Y. Matsunaga, M. Ichioka, K. Machida, Phys. Rev. B 70 (2004) 100502(R);
A.A. Golubov, A.E. Koshelev, Phys. Rev. B 68 (2003) 104503;
E. Pechenik, B. Rosenstein, B.Ya. Shapiro, I. Shapiro, Phys. Rev. B 65 (2002) 214532.
[11] H. Büttner, Yu.B. Gaididei, A. Saxena, T. Lookman, A.R. Bishop, J. Phys. A: Math. Gen. 37 (2004) 8595.
[12] See, e.g., R. Kato, Y. Enomoto, S. Maekawa, Phys. Rev. B 47 (1993) 8016;
W.D. Gropp, H.G. Kaper, G.K. Leaf, D.M. Levine, M. Palumbo, V.M. Vinokur, J. Comput. Phys. 123 (1996) 254.
[13] S.M.M. Virtanen, M.M. Salomaa, J. Phys.: Condens. Matter 12 (2000) L147.
[14] M. Abramowitz, I.A. Stegun, Handbook of Mathematical Functions with Formulas, Graphs, and Mathematical Tables, Dover, New York, 1970.
[15] S. Madsen, Yu.B. Gaididei, P.L. Christiansen, N.F. Pedersen, in: Proceedings for the Plasma 2004 Conference in Tsukuba, Japan, 2004.
[16] P.F. Byrd, M.D. Friedman, Handbook of Elliptic Integrals for Engineers and Scientists, Springer-Verlag, Berlin, 1971.